AAS 22-799

APPROXIMATING ADMISSIBLE CONTROL ONTO THE CISLUNAR HIGHWAYS FOR DETECTION AND TRACKING OF SPACECRAFT

David Schwab[*], Roshan Eapen[†], Puneet Singla[‡]

There exists a need to expand current Space Domain Awareness (SDA) architectures to account for additional challenges present in cislunar space. A scenario of particular importance is the ability to define a useful search space if custody of a cislunar spacecraft has been lost. Invariant manifold structures present in the dynamics of the circular three-body problem (CR3BP) define highways in which spacecraft must reside to transit to different regimes of the CR3BP. This paper aims to approximately define admissible controls which will enter a spacecraft onto these highways and use this estimate to define an intelligent search space.

INTRODUCTION

As reflected in the Air Force Space Command's report on the *The Future of Space 2060 & Implications for U.S. Strategy*, cislunar space will likely be an important civil, commercial, and military domain in the near future [1]. This trend is already visible in NASA's Artemis Program [2], as well as the recently accomplish or announced lunar mission by China [3, 4], Russia [5, 6], India [7], and Japan [8].

The current Space Domain Awareness (SDA) architecture has focused on objects in GEO and below [9], many of which are not applicable to the cislunar regime. There are significant challenges in the cislunar regime that will require development of new SDA algorithms and platforms, such as the AFRL xGEO space domain awareness flight experiment launching in the near future [10]. These challenges include 1) Data-sparsity from limited coverage and availability of sensor resources, 2) Low sensor signal to noise ratio (SNR) due to vast distances and atmospheric blurring effects of ground-based sensors, and 3) The sheer volume of the cislunar domain [9, 11] (roughly 1000 times the volume of the traditional SDA domain out to geosynchronous orbit). These difficult challenges are only exacerbated in the presence of non-cooperative, maneuvering target-spacecraft.

The problem of detecting and reconstructing maneuvers in data-sparse situations has received some, albeit very limited, coverage in tracking literature. Patera [12] addresses the problem of detecting maneuvers and other events (collisions, reentry, etc) in terms of statistically significant changes in orbital energy. An optimal control-based method has also been developed to reconstruct finite maneuvers [13–15]. The underlying technique for this method was first formulated in

[*]Graduate Student, Department of Aerospace Engineering, Pennsylvania State University, University Park, PA-16802, Email: dvs5558@psu.edu.

[†]Assistant Professor, Department of Aerospace Engineering, Pennsylvania State University, University Park, PA-16802, Email: rpe5185@psu.edu.

[‡]Professor, AIAA Associate Fellow, AAS Fellow, Department of Aerospace Engineering, Pennsylvania State University, University Park, PA-16802, Email: psingla@psu.edu.

1988 as the minimum model error method [16], where the control is considered to be an unmodeled deviation from the dynamics, and this deviation is minimized such that the state estimate is statistically consistent with the observations. When applied to the satellite tracking problem, this method formulates the maneuver detection process as an optimal control problem connecting two sparse measurements (two point boundary value problem) using an assumed minimum fuel control policy. These algorithms are not able to capture the many sub-optimal trajectories that can explain the same observation data and assume readily available measurements of the spacecraft. Therefore, defining a admissible region–under limited assumptions–for a spacecraft given a missed observation is needed.

As shown in previous work [17], the admissible region of a spacecraft given a simple bound on $\|\mathbf{\Delta v}\|$ may quickly grow too large to search in any practical sense and will include unlikely/low-priority trajectories such as those which leave the L_2 gateway. This work attempts to reduce these deficiencies leveraging the concept of admissible regions. This has been done in the GEO-and-below orbital domain via initial orbit determination where only tracklets returning pre-specified bounds, such as Earth-bounded orbits [18, 19], are defined. By taking advantage of the invariant manifold structures in cislunar dynamics, there exists a framework to define a set of admissible impulsive controls which produces transit trajectories of interest for a cislunar SDA architecture. This paper intends to develop that framework in the planar circular restricted three-body problem.

PLANAR CIRCULAR RESTRICTED THREE-BODY PROBLEM

This section discusses the Circular Restricted Three-Body Problem (CR3BP) and some important features of the dynamical model. In this problem, two primary masses M_1 and M_2 are restricted to follow circular Keplerian orbits about their common barycenter, and a third much smaller object with negligible mass, i.e. a satellite, moves under the influence of these two bodies. M_1 is usually taken as the larger (or more massive) primary, and M_2 is the smaller (or less-massive) primary. In the planar CR3BP, the motion of the third body is constrained to lie in the plane of the primaries. Characteristic units are defined to non-dimensionalize the problem such that the distance unit is the semimajor axis of the orbit of the second primary about the first $DU = a$, the mass unit is the total mass of the primaries $MU = M_1 + M_2$ and the time unit is selected such that the universal gravitational constant is equal to one $TU = 2\pi\sqrt{\frac{DU^3}{G \cdot MU}}$. A mass ratio μ is defined as

$$\mu = \frac{M_2}{MU}. \tag{1}$$

For the Earth-Moon system studied in this work, $\mu = 0.0122$, $DU = 384400$ km and $TU \approx 4.3425$ days. The equations of motion of the CR3BP are best represented in a rotating reference frame where the barycenter of the system is taken as the origin, and both primaries lie on the x-axis. As a consequence of non-dimensionalization, the larger primary is located at $(-\mu, 0)$, and the smaller primary at $(1 - \mu, 0)$.

The planar equations of motion are given as

$$\ddot{x} = x + 2\dot{y} - \frac{1-\mu}{r_1^3}(x + \mu) - \frac{\mu}{r_2^3}(x - (1 - \mu)) \tag{2}$$

$$\ddot{y} = y - 2\dot{x} - \frac{1-\mu}{r_1^3}y - \frac{\mu}{r_2^3}y \tag{3}$$

where state is given by $\boldsymbol{x} = [x\ y\ \dot{x}\ \dot{y}]^T$, and r_1, r_2 are the magnitudes of distance between the third body and the first and second primaries, respectively.

Equilibrium points, Periodic orbits, and Invariant Manifolds

The autonomous and conservative nature of the Hamiltonian ($\mathcal{H}$) admits a constant of motion (the Jacobi constant) as $C = -2\mathcal{H} = -|\dot{\mathbf{q}}|^2 + 2\Omega$, which is commonly used as a measure of energy in the planar CR3BP. The CR3BP admits five equilibrium points: the so-called collinear (L_1, L_2, L_3) and triangular (L_4, L_5) points based on its location in the rotating frame [20]. The triangular points are linearly stable for a mass parameter μ less than a critical value ($\mu_c = 0.0385$), and the collinear points are always linearly unstable. The curves of zero-velocity (obtained from the expression for the Jacobi constant for a particular value of μ) denote regions of the phase-space where a particle arrives with zero velocity, and therefore, cannot penetrate these curves [20].

The equilibrium points host a variety of periodic orbits in their vicinity, and dynamical systems approaches can be employed to construct them. In the planar CR3BP, the periodic orbits about the collinear equilibrium points are called Lyapunov orbits. An initial Lyapunov orbit is obtained using the linearized dynamics about the equilibrium point and using the method of differential corrections to ensure closure of the orbit [21–23]. Each periodic orbit can be identified using its time-period (T) and the Jacobi constant (C). Thus, a periodic orbit is represented as $\Gamma(T, C)$. Any specific point on the periodic orbit can be represented using a parameter $\tau \in [0, T)$ where τ is the time elapsed from an initial condition that generates the periodic orbit. Due to periodicity, $\Gamma(\tau + T) = \Gamma(\tau)$. A continuations process is usually used to obtain Lyapunov orbits at different Jacobi constant values [24].

Similar to an equilibrium point, which are fixed points of a flow, a point on the periodic orbit is represented as a fixed point on a stroboscopic map [25]. The linearized dynamics about this fixed point are obtained from the monodromy matrix $\mathcal{M}$, which is the state transition matrix at one time period, and it provides insights into the flow in the neighborhood of the periodic orbit. Following from Floquet theory, stability of a periodic orbit may be examined using the eigenvalues of $\mathcal{M}$ are used to define the stability of the periodic orbit (analogous to linear stability analysis for fixed points on a map). Using this tool, eigenvalues and eigenvectors may be generated for any point on the periodic orbit. The collinear Lyapunov orbits–of the type studied in this work– has a saddle subspace. This subspace is represented by stable and unstable manifolds, which are nonlinear generalizations of these subspaces. These stable and unstable manifolds act as separatrices to the periodic orbit; therefore, trajectories that lie on the manifold, tend towards or away from the periodic orbit as $t \to \infty$. Trajectories that lie inside the manifold always stay inside, and those that lie outside, remain outside for all time. They serve as phase-space structures that transport particles between the neighborhood of the primaries [25, 26].

METHODOLOGY

Previous work [17] has shown that uniform bounds on $\|\Delta\mathbf{v}\|$ may lead to very large reachability, therefore limiting the utility for a cislunar SDA architecture. Figure 1 shows randomly sampled maneuvers such that $\|\Delta\mathbf{v}\| \in [0, 30]$ (m/s) and the maneuver occurs between $[45^\circ, 25^\circ]$ with respect to L_2. After 192 hours, the reachable space stretches to approximately 130,000 km; from the lunar vicinity to beyond the L_2 gateway. An observer is likely more concerned with trajectories which transit from L_2 and through the Lunar plane; removing the need to define the reachable set outside the L_2 gateway. A viable admissible region to impart in this scenario is trajectories which pass

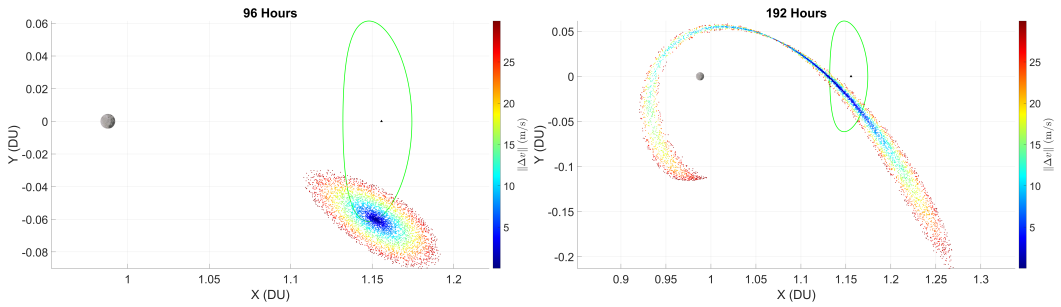

Figure 1. Propagation of sampled maneuvers with $\|\Delta\mathbf{v}\| \in [0, 30]$ (m/s) and at maneuver locations between $[45°, 25°]$ with respect to L_2.

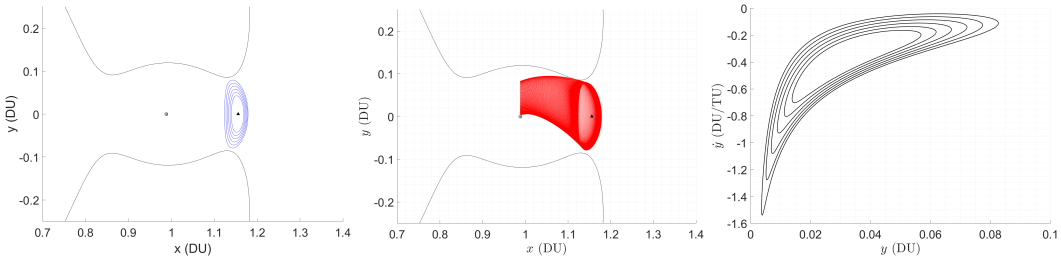

(a) Lyapunov Orbits (b) Invariant Manifolds (c) Poincare Surface

Figure 2. Exemplar Lyapunov orbits, their invariant manifolds, and the manifold curves on a Poincaré surface of section.

through the lunar plane; similar to defining an Earth-bound orbit as an admissible region for initial orbit determination in the works [18, 19]. Therefore, the objective of this work is to define a set of admissible $\Delta\mathbf{v}$ which enter a spacecraft in a nominal L_2-Lyapunov orbit onto the admissible region defined as the *cislunar highway* between L_2 and the Lunar plane.

The invariant manifold tubes defined by the Lyaponuv orbit families in L_1 and L_2 separate transit and non-transit solutions. For instance, all trajectories at a certain energy level that pass through the L_2 gateway lies within the interior of the invariant manifold tubes of an L_2 Lyapunov orbit at that energy level [27]. In this way, the invariant manifold tubes act as part of the *cislunar highway* system which constrain the transit of spacecraft. A common tool for analysis is a Poincaré Surface of Section (PSS) which allows for the reduction of a systems dimensionality by at least one and simplifies the study of specific properties of the flow [28]. Figure 2 shows L_2 Lyapunov orbits at different energy levels, the invariant manifold tubes of the maximum orbit energy, and the manifold curves on the Poincaré surface of section.

Koon et al. [27] use the intersection of these manifolds on a PSS to define spacecraft trajectories which transit through the L_2 and then L_1 gateways and into the interior of the system. Using the same principles, the intersection of the invariant manifolds at maximum energy level on the PSS will provide an upper bound on a spacecraft reachability set on that surface. A Poincaré surface of section that captures the transit from L_2 through the Lunar plane is

$$U = \{(y, \dot{y}) \mid x = 1 - \mu,\, y > 0,\, \dot{x}(y, \dot{y}, C) < 0\}. \tag{4}$$

With utility of invariant manifolds and their intersection on the PSS established, the intersection

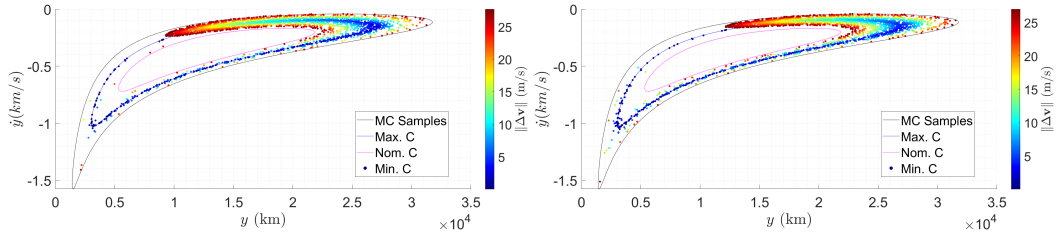

(a) Maneuver at 45° (b) Maneuver at -5°

Figure 3. Intersection on the PSS given a bounded $\|\Delta \mathbf{v}\|$.

of random, bounded maneuvers with the PSS is investigated. Assume the target spacecraft is on some nominal Lyapunov orbit about L_2 at a $C = C_{nom}$ and performs a bounded maneuver which defines a change in Jacobi constant:

$$\Delta C = C - C_{nom} = -\|\mathbf{\Delta v}\|^2 - 2\|\mathbf{\Delta v}\|\|\mathbf{v}_{nom}\|\cos\theta, \tag{5}$$

where $\theta = \angle(\mathbf{\Delta v}, \mathbf{v}_{nom})$. Holding $\Delta \mathbf{v}$ constant and given a smaller Jacobi constant means a larger orbit (i.e. $C_{min} > C_{nom} > C_{max}$), the maximum change in C occurs at $\theta = 0$ while the minimum occurs at $\theta = 180^\circ$, therefore defining C_{max} and C_{min}, respectively. Figure 3 shows the intersection of randomly sampled bounded maneuvers. At the maneuver locations in Figure 3, fixing $C_{max} - C_{nom} \approx -0.0065$ gives a bound of $\max(\|\Delta \mathbf{v}\|) \approx 30$ m/s. While it is mathematically true that the invariant manifold intersection of the PSS at C_{max} provides the upper bound on a trajectory's intersection, a lower bound may be imposed heuristically on the PSS given a bounded $\|\Delta \mathbf{v}\|$ as evidenced by Figure 3. The curves on the Poincaré surface of section for the minimal and maximum C may be used to approximate the accessible region on U given a bounded $\|\Delta \mathbf{v}\|$.

From this bounded region on the PSS, points may be generated as possible destinations for a maneuvering spacecraft in a given L_2-Lyapunov orbit intending to pass through the Lunar plane. Therefore, two-point boundary value problems (TPBVPs) from sample initial positions to sample final positions are posed. The solution of these TPBVPs are computationally expensive and therefore necessitates a computationally efficient approximation for rapid generation of the admissible region. By fitting a surface to the solutions of these TPBVPs, then the admissible control which will enter a spacecraft onto this tubes–or highways–is approximated using simple polynomial basis functions. The benefits of this approach include allowing a SDA architecture to place uncertainty on the intent of an intelligently maneuvering spacecraft, prioritize regions of the reachable set with a low ToF to the PSS, and further reduce this admissible region through additional analysis on the PSS.

Approximating Surfaces using Basis Functions

First, the problem of approximating a m-dimensional surface as a function of an n-dimensional input is introduced. The objective becomes finding the coefficients of basis functions, $\mathbf{P} \in \mathcal{R}^{m \times \alpha}$, such that

$$\mathbf{f}(\mathbf{x}) \approx \mathbf{P}\boldsymbol{\phi}(\mathbf{x}), \tag{6}$$

where $\mathbf{f} : \mathcal{R}^n \to \mathcal{R}^m$, $\mathbf{x} \in \mathcal{R}^n$, and $\boldsymbol{\phi}(\mathbf{x}) : \mathcal{R}^n \to \mathcal{R}^\alpha$ is a user-specified library of basis functions. This work follows a least squares formulation–defined in Appendix A–minimizing the weighted 2-norm error over the entire domain.

The Legendre polynomials, $\mathcal{L}_{\alpha_i}(x_i) \in \mathcal{P}_{\alpha_i}$, are used with $\rho(x_i) = 1$ for all input dimensions $i = 1, ..., n$ to construct the basis function library as described in Appendix A. The inner products in this formulation may be calculated using numerical methods. In this work, the Gauss-Legendre quadrature scheme is used for each input component and combined using the tensor product. Letting α_i be the maximum degree of the polynomial in the i-component, then the minimum number of quadrature points must be $n_{q,i} = \alpha_i + 1$ given Gauss-Legendre quadrature can integrate degree $2n - 1$ polynomials exactly and the maximum polynomial integrated in Equation (14) is $2\alpha_i$.

Approximating Invariant Manifold curves on a Poincaré surface A state vector on the Lyapunov orbit can be uniquely defined by the Jacobi constant,$\Psi_1 \in [C_{max}, C_{min}]$, and the ratio of time passed to the period, $\Psi_2 \in [0,\ 1]$. The vector $\mathbf{\Psi}$ then constitutes the input vector, $\mathbf{x}$, in Equation (6). An unstable manifold may be generated from this point and propagated to the PSS, which constitutes the output map, $\mathbf{f}(\mathbf{x})$, in Equation (6). Therefore, the problem of defining the PSS approximation is

$$\begin{bmatrix} y \\ \dot{y} \end{bmatrix} \approx \mathbf{P}\boldsymbol{\phi}\left(\begin{bmatrix} \Psi_1 \\ \Psi_2 \end{bmatrix}\right). \tag{7}$$

For this work, $\Psi_2 = 0$ corresponds to the position on the Lyapunov orbit along the x-axis and closest to the Moon, and the manifolds for determining the true y and $\dot{y}$ are generated with a 20 km step off distance. Additionally, the quadrature points are generated such that $\bar{\mathbf{\Psi}} \in [-1, 1]$ for numerical purposes, but are easily mapped to $\mathbf{\Psi}$ via min-max de-normalization.

Approximating Maneuvers onto the Cislunar Highway Equation Equation (11) allows for the direct generation of points which lie between the invariant manifold curves of the minimal and maximum C on the PSS. This subspace defines a conservative bound on reachable points as shown heuristically in Figure 3. Therefore, by generating samples within the subspace on the Poincaré surface and samples of the target's position at maneuver time, a set of TPBVPs is formed.

Given samples of $\mathbf{\Psi}_i$ and samples of target position at maneuver time, $\mathbf{r}_i$, the formulation of a single TPBVP is such that

$$\left.\begin{aligned} x_{PSS} &= 1 - \mu \\ \begin{bmatrix} y_{PSS} \\ \dot{y}_{PSS} \end{bmatrix} &= \mathbf{P}\boldsymbol{\phi}(\mathbf{\Psi}_i) \\ \mathbf{r}(\beta_i) \end{aligned}\right\} \text{ is specified,} \qquad \left.\begin{aligned} \Delta v_x \\ \Delta v_y \\ \sigma := \text{Time of Flight} \end{aligned}\right\} \text{ is free,} \tag{8}$$

where β_i is the angle of the position vector with respect to L_2. Under these assumptions, one may solve this TPBVP using a shooting method formulation where the trajectory is propagated from $\mathbf{r}(\beta_i)$ with an initial guess for $\Delta\mathbf{v}$. The initial guess is then corrected using first-order sensitivities and iterated until convergence

$$\begin{bmatrix} \delta x_{PSS} \\ \delta y_{PSS} \\ \delta \dot{y}_{PSS} \end{bmatrix} = \begin{bmatrix} \frac{\partial x_{PSS}}{\partial \Delta v_x} & \frac{\partial x_{PSS}}{\partial \Delta v_y} & \frac{\partial x_{PSS}}{\partial \sigma} \\ \frac{\partial y_{PSS}}{\partial \Delta v_x} & \frac{\partial y_{PSS}}{\partial \Delta v_y} & \frac{\partial y_{PSS}}{\partial \sigma} \\ \frac{\partial \dot{y}_{PSS}}{\partial \Delta v_x} & \frac{\partial \dot{y}_{PSS}}{\partial \Delta v_y} & \frac{\partial \dot{y}_{PSS}}{\partial \sigma} \end{bmatrix} \begin{bmatrix} \delta \Delta v_x \\ \delta \Delta v_y \\ \delta \sigma \end{bmatrix}. \tag{9}$$

The particular formulation of the shooting method used in this work is known as stabilized continuation, which provides adaptive step-size selection through use of an ODE propagator, such as MATLAB's `ode45`, among other benefits [29, 30]. A brief introduction to this method is provided in Appendix B.

Combining the Manifold Curve Approximation and the TPBVP

The manifold approximation and the posed TPBVPs give a framework to develop a direct approximation to the admissible control which will enter the target spacecraft onto the cislunar highway through the lunar plane. The approximation to the invariant manifold curves between set levels of C are defined via the polynomial approximation method proposed in this work. Therefore, y_{PSS} and $\dot{y}_{PSS}$ between those curves may be generated directly by sampling in $\mathbf{\Psi}$. The PSS approximation allows for the use of quadrature points in the TPBVP approximation by directly generating points between the bounds and therefore avoiding the sample rejection method that would have to be used otherwise.

Gauss-Legendre quadrature points, $\boldsymbol{\zeta} \in [-1, 1]$, are generated under the assumption that

$$\begin{aligned} \zeta_1 &= \frac{\beta}{\pi} \\ \zeta_2 &= \bar{\mathbf{\Psi}}_1 \\ \zeta_3 &= R(\bar{\mathbf{\Psi}}_2) \end{aligned} \tag{10}$$

where $R(\bar{\mathbf{\Psi}}_2)$ is a user defined map to ensure that the solution surface is continuous and that the resulting $\|\Delta\mathbf{v}\|$ are reasonable. This can be done because $\bar{\mathbf{\Psi}}_2$ is a cyclic variable, therefore this mapping is analogous to unwrapping angle variables or adding a phase shift. An examination of the effects of the mapping is provided later in this work. These quadrature points and mappings will allow for the direct approximation of Δv_x, Δv_y, and σ via the same least squares approximation technique used to approximate the manifold curves on the PSS. For the TPBVP solution surface, the mapping is such that

$$\begin{bmatrix} \Delta v_x \\ \Delta v_y \\ \sigma \end{bmatrix} \approx \mathbf{P}\boldsymbol{\phi}\left(\begin{bmatrix} \zeta_1 \\ \zeta_2 \\ \zeta_3 \end{bmatrix} \right). \tag{11}$$

RESULTS

Investigations of the regression fit to the Poincaré surface and the TPBVP solutions are discussed. The Jacobi constants discussed are such that the $C_{max} = 3.1558$ and $C_{min} = 3.1674$ given that lower numeric values for C correspond to larger orbits.

Approximating Invariant Manifold curves on a Poincaré surface Figure 4(a) shows the ground truth and approximation for both quadrature points used for training and the Monte Carlo points used for testing at $\alpha_1 = 3$ or $\alpha_2 = 30$. The qualitative relationship between the outputs–y and $\dot{y}$ curve on the PSS–to the components of inputs–$\mathbf{\Psi}$–is evident. The outputs oscillate with respect to Ψ_2 while the amplitude is affected by Ψ_1.

Figure 4(b) shows the errors in the approximation for both the quadrature and the Monte Carlo points. The errors in y stay relatively constant with respect to Ψ_1, but they oscillate slightly with respect to Ψ_2. This is likely due to the high order polynomials used in Ψ_2. The errors in $\dot{y}$ show a similar result, except that the errors with respect to Ψ_1 increase near $\Psi_1 = 3.155$. As shown in Figure 4(a), the sharper curve in that region as compared to $\Psi_1 = 3.17$ likely induces this increased error due to the local training data sparsity and surface shape.

A study varying α_2 while keeping the number of quadrature points in Ψ_2 fixed at 32 is conducted. Figure 5 shows the evolution of the maximum percent error and the RMSE for training and testing

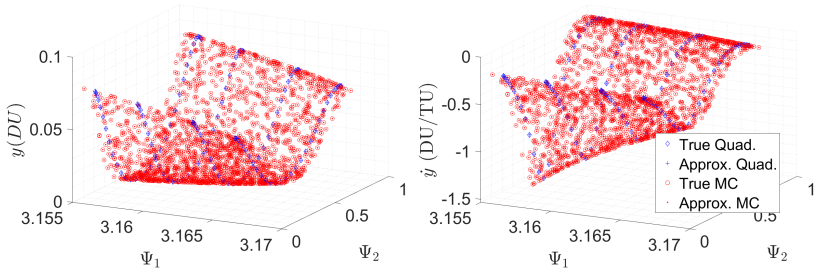

(a) Approximation outputs.

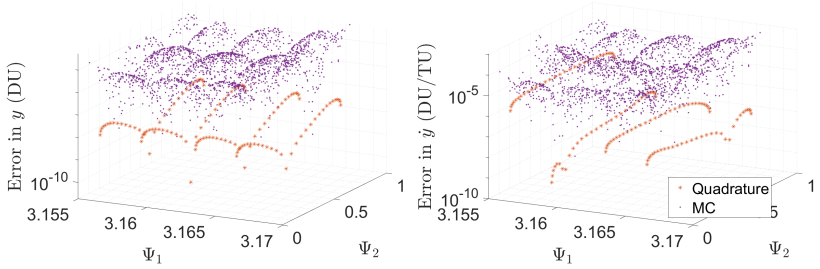

(b) Absolute value of approximation errors.

Figure 4. Approximation for the PSS $[y,\ \dot{y}]^T \approx \mathbf{P}\boldsymbol{\phi}(\boldsymbol{\Psi})$ for $\alpha_1 = 3$ and $\alpha_2 = 30$.

points. For training points, the errors for both output components generally decrease as α_2 increases. For testing points, the errors level off relatively quickly for y, but only begin to level off as α_2 approaches the mid-twenties for $\dot{y}$. This is likely a reflection of the increasingly steep dip in the $\dot{y}$ discussed in respect to Figure 4(a).

The magnitude of the resulting coefficients versus the order of the basis functions and α_2 is shown in Figure 6. In general, the coefficient magnitude decreases as the order increases, which means the approximation relies on lower order terms. Additionally, the rational for the leveling off of testing errors in Figure 5 is realized. For y, the scale of the coefficients as α_2 increases and quickly becomes many orders of magnitude below that of the lower order terms. This trend is not as drastic in the $\dot{y}$ coefficients and therefore is the likely reasoning for the leveling off of errors at a increased α_2.

Combining the Manifold Curve Approximation and the TPBVP

With an accurate approximation to the PSS, the solution surface to the set of TPBVPs between a nominal orbit and the PSS may be approximated. A maneuver window is determined and the mappings in equation Equation (10) are defined a priori. The number of quadrature points selected are 4, 6, and 23 in ζ_1, ζ_2, and ζ_3, respectively. The phase shift, $R(\bar{\boldsymbol{\Psi}}_2)$ in Equation (10), is determined by taking as the $\Delta\mathbf{v}$ the velocity component of the invariant manifold at the lower bound of the maneuver location, β, and propagating the to the PSS. The value of Ψ_2 at that location determined $R(\bar{\boldsymbol{\Psi}}_2)$. For compactness, a complete study of only the maneuver window $\beta \in [45°, 25°]$ is shown in this section. The Monte Carlo points are generated such that 10 random β are generated and 500 points are generated on the PSS at each β. This ensured that each Monte Carlo sample had an initial guess which converged to a solution in the stabilized continuation method.

The TPBVP solution surfaces are shown for the quadrature points and Monte Carlo points in Figure 7. Remembering the mapping in Equation (10), the effects of each input variable is clearly

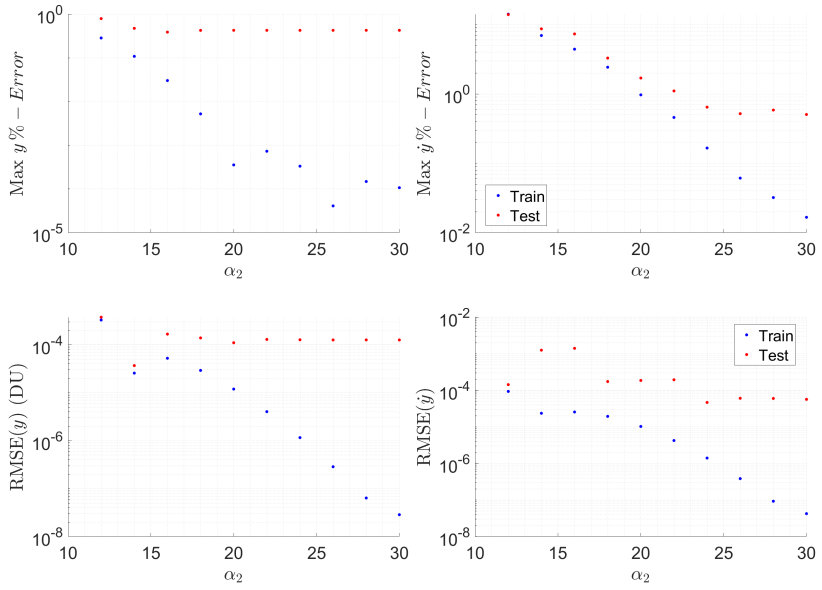

Figure 5. Approximation Errors as a function of Polynomial Order.

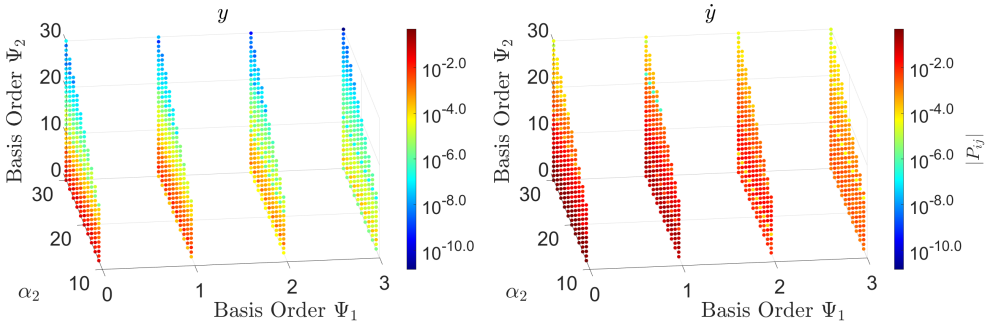

Figure 6. Coefficient magnitude as a function of the polynomial order in Ψ_1 and $\Psi 2$ across increasing α_2.

visible in Figure 7(a). The $\Delta\mathbf{v}$ are obviously lower order functions in ζ_1 and ζ_2 and a higher order function in ζ_3. As $\zeta_3 \to -1$, there is a near exponential increase in Δv_x and a smaller but similar trend in Δv_y. At a fixed ζ_1 and ζ_3, the $\Delta\mathbf{v}$ components follow a near linear relationship. The maneuver location, related to ζ_1, essentially adds thickness to the surface, which becomes significant as $\zeta_3 \to -1$. The ToF approximation is similar to a flat plate with very small variations with respect to ζ_1 and ζ_2, near-linear increase as $\zeta_3 \to 1$, and with a small thickness added through ζ_1.

Figure 8 reflects the coefficients for each output variable and the order of their corresponding basis function. The magnitude drops nearly an order of magnitude at each increase in polynomial order in ζ_1 for Δv_y and ToF . This trend is less evident in Δv_x because of its increased variation with respect to ζ_1 as $\zeta_3 \to -1$. In general, the coefficient order of magnitude also steadily decreases as ζ_2 increase, though at a seemingly slower pace. Finally, the strong relationship with respect to ζ_3 is evident as the coefficients do not show a multi-magnitude decrease until the order of the corresponding basis functions pass 10, generally. This is especially evident in Δv_x, again most likely due to its near-exponential increase in as $\zeta_3 \to -1$.

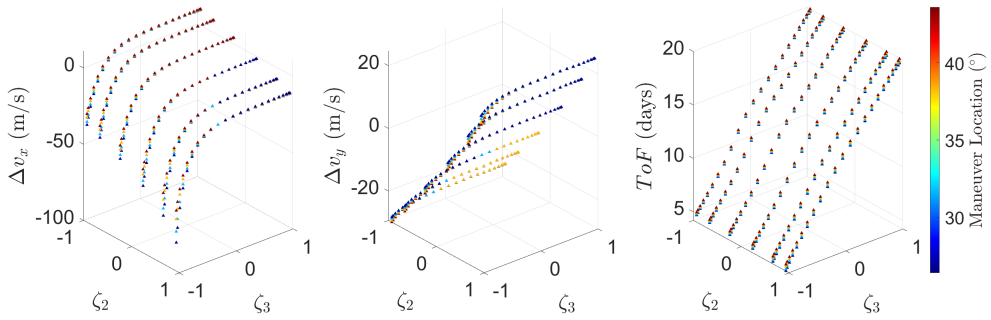

(a) Quadrature Points.

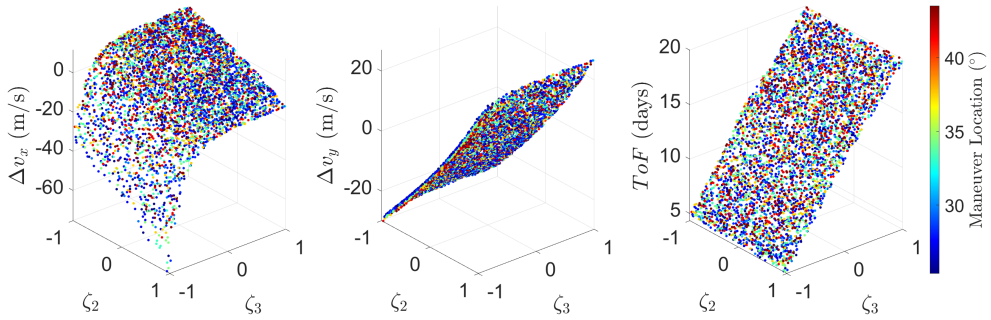

(b) Monte Carlo points.

Figure 7. The surface for $\Delta\mathbf{v}$ and ToF for quadrature and Monte Carlo points.

Approximation accuracy versus the ground truth solutions for $\|\Delta\mathbf{v}\|$, $\angle(\Delta\mathbf{v}_{GT}, \Delta\mathbf{v}_{APP})$, and ToF are shown in Figure 9. The $\|\Delta\mathbf{v}\|$ approximation errors are between two and three orders-of-magnitude below that of the ground truth. The pointing error is greater than $0.01°$ only for points with $\|\Delta\mathbf{v}\| \leq 1$ m/s due due to the increased sensitivity to directional errors as the vector magnitude decreases. Additionally, notice that many of the angles take on distinct values hovering around 115 and 295, which is why the entire PSS surface is not captured when propagated random $\Delta\mathbf{v}$ in Figure 3. Finally, the ToF errors are on the order of a few minutes while the ground truth ToF is bewteen 4 and 20 days.

Figure 10(b) depicts the $\|\Delta\mathbf{v}\|$ and ToF as a function of the position of the ground truth solution on the PSS. Note the region of steep discontinuity in both values. The location of this discontinuity

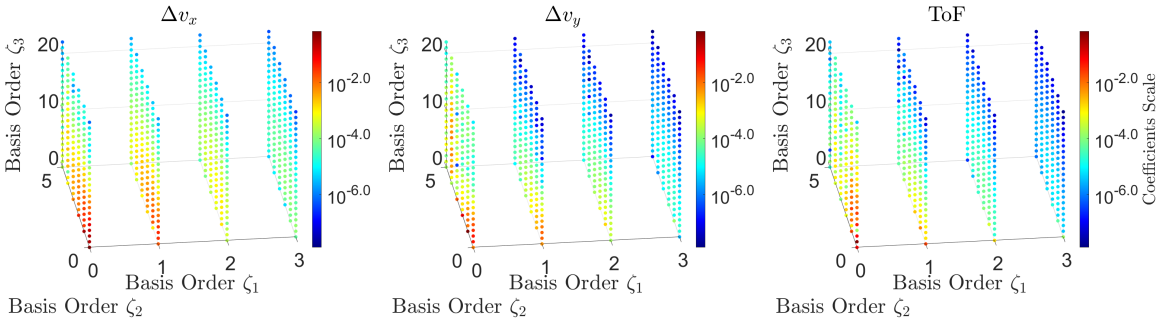

Figure 8. Coefficient magnitude as a function of basis order in each input component.

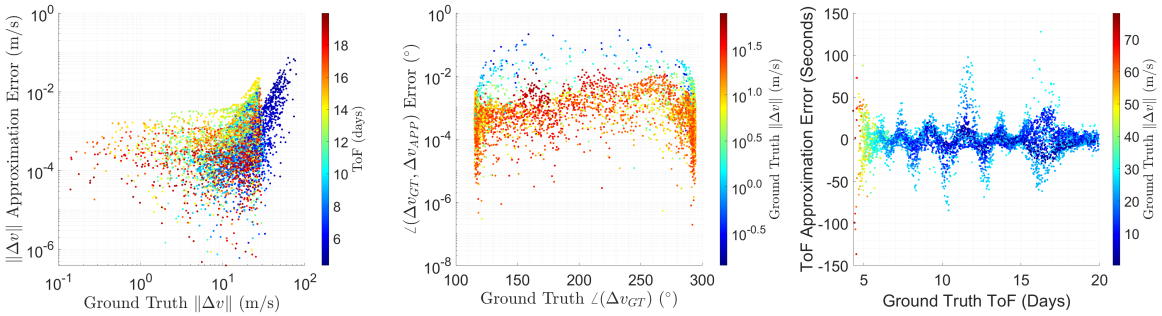

Figure 9. Approximation errors of $\Delta\mathbf{v}$ and ToF versus their ground truth.

is shifted by the selection of $R(\bar{\mathbf{\Psi}}_2)$ as this value determines how much of the short ToF region is captured; more about this result is presented later in this work. The errors of the approximated $\|\Delta\mathbf{v}\|$ and ToF with respect to the position on the PSS are shown in Figure 10(b). In general, the largest errors occur in regions requiring higher $\|\Delta\mathbf{v}\|$, which occurs at the edges of the minimum and maximum energy bounds and to the $+y$-direction of the discontinuity. Additionally, there is an area of increased error in the $y < 10,000$ km region, which is most visible on the right of Figure 10(b). The area of this region is comparatively large to the rest of the PSS, therefore the errors are likely caused by a sparsity in ζ_2 given this parameter is analogous to the radial distance.

The accuracy of propagating the approximation may be broken down into two question: 1) how accurate is the $\Delta\mathbf{v}$ approximation in reaching the ground truth location on the PSS (Figure 11(a)), and 2) how accurate is the ToF approximation when propagated the true $\Delta\mathbf{v}$ (Figure 11(b)). The accuracy of the full approximation–ToF and $\Delta\mathbf{v}$–is shown on the left of Figure 11. Note that the points on Figure 11(a) represent the ground truth solution and the color represents the approximation error of the full state while the points in Figure 11(b) represent the propagated approximations. The errors are large when using the full approximation. This is especially true in the long ToF region, which also corresponds to the region closest to the Moon. Errors reduce to approximately $10^{-2.5}$ or less when the approximated $\Delta\mathbf{v}$ is propagated exactly to the PSS as shown on the the right of Figure 11(b). A similar trend is evident when the approximated ToF is used to propagate the ground truth $\Delta\mathbf{v}$, though errors are on the order of $10^{-1.5}$ or less. The largest approximation errors occurring closest to the Moon as this region is more sensitive to ToF errors and coincidentally the region with longest ToF, where errors have more time to accumulate.

Figure 12 shows the propagation of 5000 randomly generated samples for the maneuver window $\beta \in [45°, 25°]$. The simulation time starts at the beginning of the maneuvering window. The pattern of propagation looks similar to that of a twisting ribbon, i.e. dense regions as shown in the light blue region at 192 hours and dispersed regions as shown below the Moon at 192 hours. The short ToF solutions depart from the nominal orbit quickly, while the high ToF solutions collect along a curve intersecting the nominal orbit. That curve expands and contracts along the nominal orbit path as a function of time.

COMMENTS ON PROPOSED METHOD

This section will expand on various aspects of this work including the examination of accuracy across multiple windows, the effects associated with the user chosen $R(\bar{\mathbf{\Psi}}_2)$, and limitations of the proposed method.

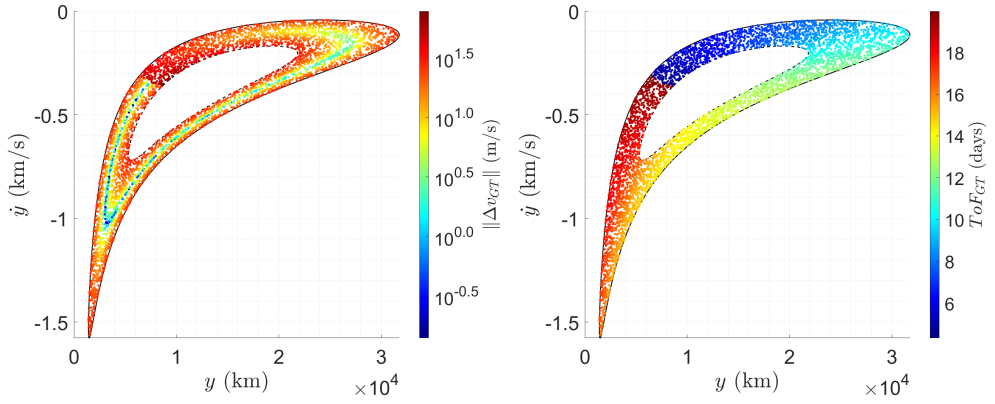

(a) Ground truth values.

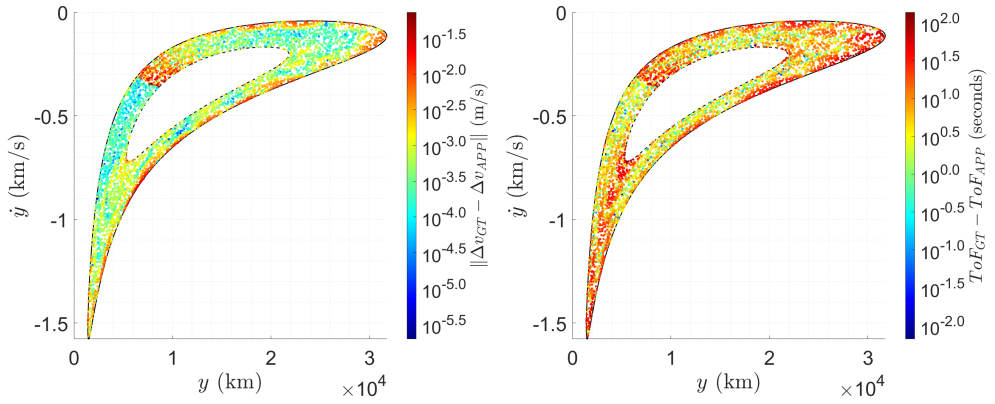

(b) Approximation errors.

Figure 10. Ground truth values and approximation errors in relation to location on the PSS.

Survey of Multiple Maneuver Windows

A survey of the approximation accuracy across various β ranges is shown in Figure 13. The trends discussed for Figure 9 are also present here. However, maximum approximation errors increase going from $\beta \in [25°, 45°]$ to $\beta \in [-5°, 15°]$, which is most evident by examining the ToF errors in Figure 13(c). The maximum $\|\Delta\mathbf{v}\|$ solution also increases, following the same trend. Therefore, the increase in error can be explained via the authors' selection of $R(\bar{\mathbf{\Psi}}_2)$ in each maneuver window. Recalling the discussion regarding Figure 10(a), the of $R(\bar{\mathbf{\Psi}}_2)$ determines how much of that high-$\|\Delta\mathbf{v}\|$/low-ToF region is captured. This region also results in higher approximation errors.

Effects of $R(\bar{\mathbf{\Psi}}_2)$

The effects of the user choice in $R(\bar{\mathbf{\Psi}}_2)$ is investigated by examining the overlapping β windows. Figure 14(a) shows a 3D scatter plot with ToF as the z-axis and $\|\Delta\mathbf{v}\|$ encoded with a color bar for the two windows $\beta \in [25°, 45°]$ and $\beta \in [15°, 35°]$. Each window represents two different approximations and has different $R(\bar{\mathbf{\Psi}}_2)$. The effect of the user choice in $R(\bar{\mathbf{\Psi}}_2)$ is evident by examining the overlapping region as shown in Figure 14(b). Here, there are two distinct regions: 1) a short ToF region with generally larger $\|\Delta\mathbf{v}\|$, and 2) a long ToF region with generally smaller $\|\Delta\mathbf{v}\|$. The selection of $R(\bar{\mathbf{\Psi}}_2)$ determines the snapshot of the continuous spirals shown in Figure 14(a). If

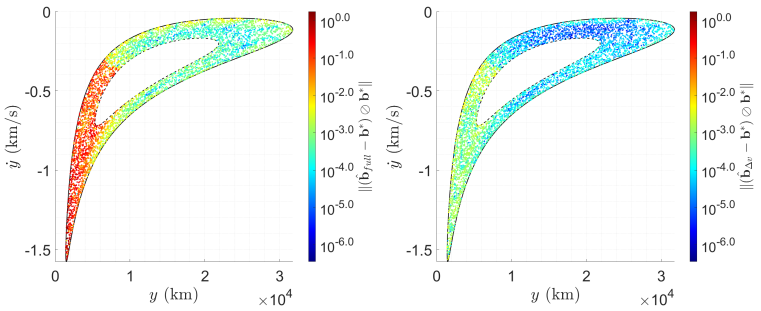

(a) $\Delta \mathbf{v}$ accuracy with approximated (left) and true (right) ToF .

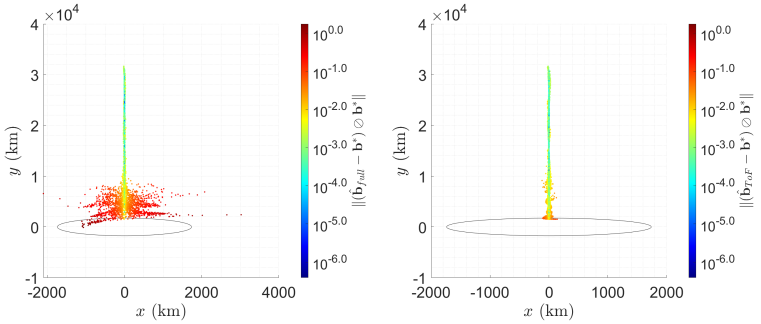

(b) ToF accuracy with approximated (left) and true (right) $\Delta \mathbf{v}$.

Figure 11. Effects of propagating the $\Delta \mathbf{v}$ and ToF estimations and accuracy with respect to the ground truth solution.

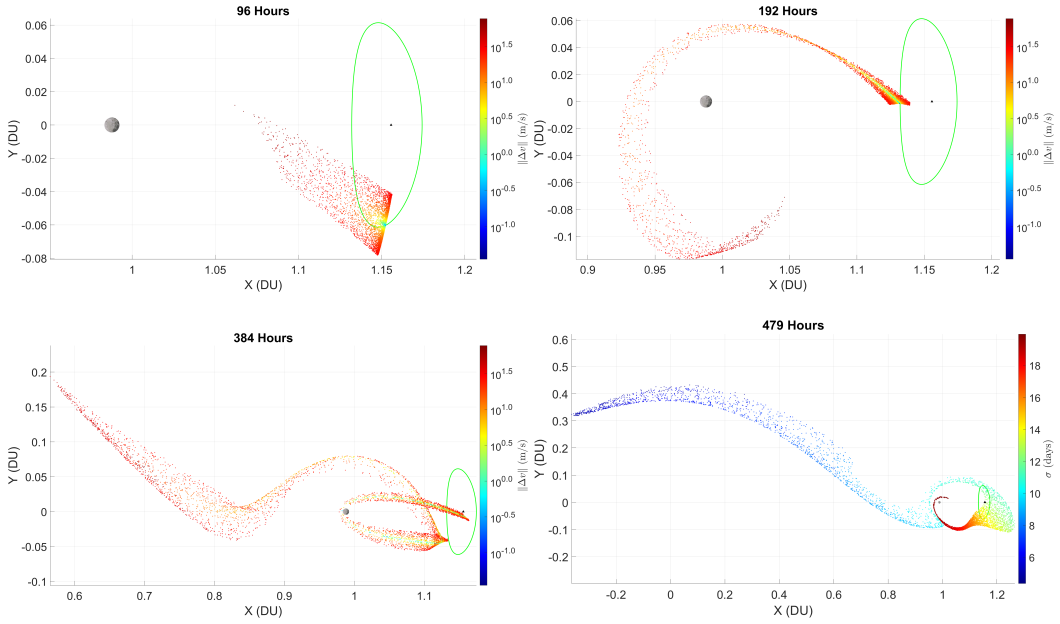

Figure 12. The propagation of 5000 randomly generated samples for $\beta \in [45°, 25°]$.

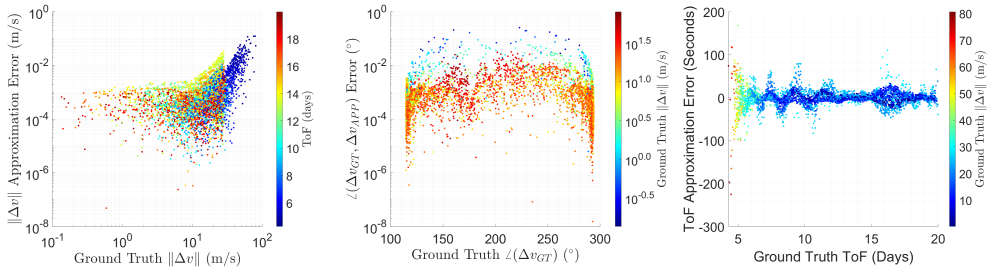

(a) $\beta \in [15°, 35°]$.

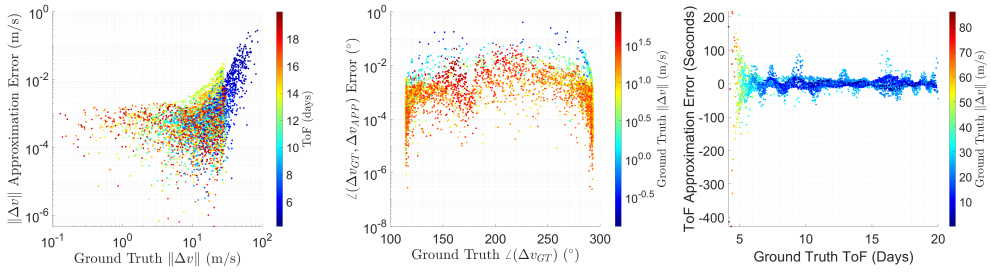

(b) $\beta \in [5°, 25°]$.

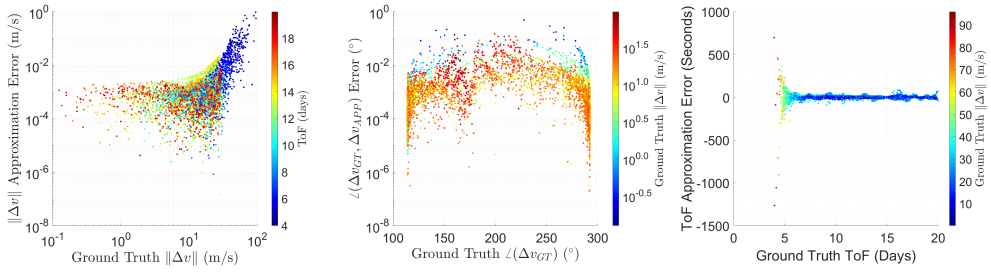

(c) $\beta \in [-5°, 15°]$.

Figure 13. Analysis of approximation accuracy across multiple windows.

the user is interested in limiting the maximum $\|\Delta\mathbf{v}\|$ presented in the approximation, then judicious selection of $R(\bar{\mathbf{\Psi}}_2)$ is required. Additionally, for the β windows, there are selections which include $\|\Delta\mathbf{v}\|$ on the same order of magnitude as the nominal orbit velocity. This results in an ill-posed TPBVP which the stabilized continuation method cannot solve.

Limitations of Underlying Assumptions

The selection of $R(\bar{\mathbf{\Psi}}_2)$ is not the only way an ill-posed TPBVP may be formed. As shown in Figure 15, the assumption that the intersections of the invariant manifolds provide conservative bounds on the reachable region does not hold for every maneuver location on the nominal orbit. The issue in this region is that the of the velocity in the nominal orbit in certain regions is close to or below the defined maximum $\|\Delta\mathbf{v}\|$. These regions violate the bounds set forth in this work and result in ill-posed TPBVP.

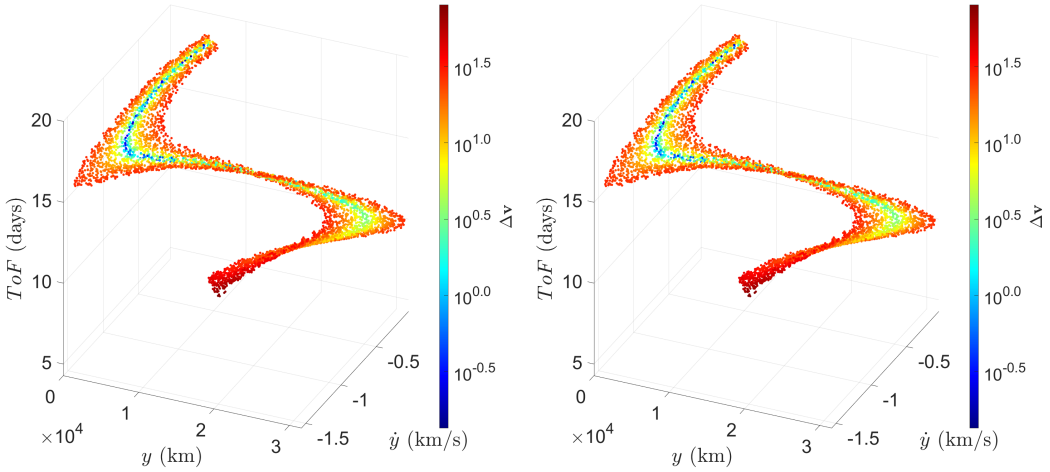

(a) Maneuver $\beta \in [25°, 45°]$ (left) and $\in [15°, 35°]$ (right).

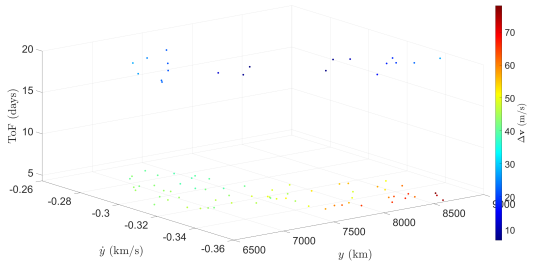

(b) Overlapping region for maneuvers $\beta \in [25°, 35°]$

Figure 14. A 3D plot of the PSS with ToF as the z-axis for the overlapping maneuver windows: $\beta \in [25°, 45°]$ and $\beta \in [25°, 35°]$.

CONCLUSIONS

In summary, the objective of this paper is to determine an admissible control region which is defined as the $\Delta\mathbf{v}$ which enters the spacecraft onto a transit trajectory from L_2 and through the Lunar plane. The authors leverage the fact that invariant manifold's intersection on a specific Poincaré surface of section provides an upper bound for all trajectories at or below the manifold's energy. The intersection of these manifolds are approximated as polynomial functions of energy and the time-to-period ratio of the original Lyapunov orbit using a least squares procedure. The imposed upper bound on energy limits $\|\Delta\mathbf{v}\|$ capabilities. A heuristic lower bound may be imposed–under certain assumptions–through the intersection of a manifold at a lower energy level. These bounds provide a region to define a set of TPBVP which enter the spacecraft onto the cislunar highway through the lunar plane. The solution surface of this set of TPBVPs is then approximated using polynomial basis functions and the same least squares procedure.

The surface fit for the manifold intersections on the PSS provided sub-1% maximum error in y and $\dot{y}$. A survey of the maximum polynomial order in the cyclic parameter, Ψ_2, has shown that high order basis functions are required to achieve that accuracy. The surface fit for the TPBVP solutions to the PSS are mostly accurate to 10^{-2}-10^{-3} in $\Delta\mathbf{v}$ and provide ToF errors on the order of a few minutes. The accuracy of propagating these approximations is examined under the assumption that the approximated $\Delta\mathbf{v}$ is propagated exactly to the PSS and the ToF is used to propagate

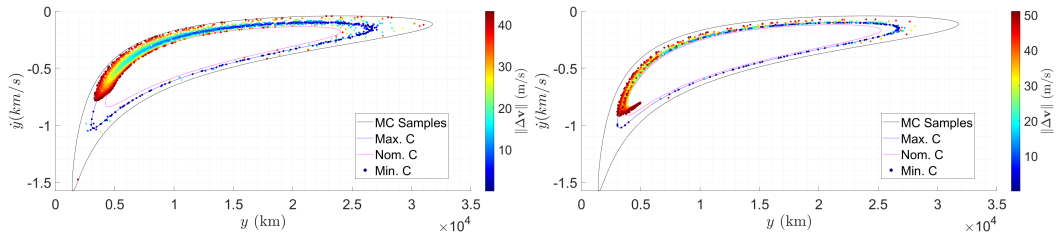

(a) Maneuver at 90° (b) Maneuver at 100°

Figure 15. Maneuver regions inducing ill-posed TPBVPs due to multiple solutions with differing ToF .

the exact $\Delta\mathbf{v}$. Under these assumptions, the propagted $\Delta\mathbf{v}$ approximation is able to achieve the boundary condition errors generally below $10^{-2.5}$, while the propagated ToF approximation errors are generally below $10^{-1.5}$.

Additionally, selecting an appropriate $R(\bar{\mathbf{\Psi}}_2)$ a priori is important to ensure a well-posed TPBVP in the region of interest and to limit the maximum magnitude of the returned $\Delta\mathbf{v}$ solutions. The TPBVP solution surface approximation is used to generate samples which are then numerically propagated and represent a large subset of trajectories originating from an nominal Lyapunov orbit and transiting through the lunar plane.

ACKNOWLEDGMENT

This material is based upon work supported jointly by the AFOSR grant FA9550-20-1-0176, FA9550-22-1-0092, as well as the DoD SMART Scholarship Program.

APPENDIX A

This work follows a least squares formulation which minimizes the weighted 2-norm error over the entire domain such that

$$\begin{aligned} J &= \frac{1}{2}\int_{\Omega} \left(f_j(\mathbf{x}) - P_{jk}\phi_k(\mathbf{x})\right)\left(f_j(\mathbf{x}) - P_{jk}\phi_k(\mathbf{x})\right)\rho(\mathbf{x})d\mathbf{x} \\ &= \left\langle f_j(\mathbf{x}) - P_{jk}\phi_k(\mathbf{x}),\, f_j(\mathbf{x}) - P_{jk}\phi_k(\mathbf{x})\right\rangle_{\rho(\mathbf{x})}, \end{aligned} \tag{12}$$

where $\rho(\mathbf{x})$ denotes the weighting function, and $\mathbf{p}^T$ make up the rows of $\mathbf{P}$ in Equation (6).

The solution follows by taking $\frac{\partial J}{\partial c_{js}} = 0$, which gives

$$\left\langle f_j(\mathbf{x}),\, \phi_s(\mathbf{x})\right\rangle_{\rho(\mathbf{x})} = P_{jk}\left\langle \phi_k(\mathbf{x}),\, \phi_s(\mathbf{x})\right\rangle_{\rho(\mathbf{x})} \tag{13}$$

and can now be expressed in matrix notation such that

$$\begin{gathered} \mathbf{A} = \mathbf{PB} \\ A_{js} = \left\langle f_j(\mathbf{x}),\, \phi_s(\mathbf{x})\right\rangle_{\rho(\mathbf{x})}, \quad B_{ks} = \left\langle \phi_k(\mathbf{x}),\, \phi_s(\mathbf{x})\right\rangle_{\rho(\mathbf{x})} \end{gathered} \tag{14}$$

$\mathbf{B}$ becomes the numerically desirable diagonal matrix if orthogonal polynomials are chosen. In any case, the coefficient matrix may be solved such that

$$\mathbf{P} = \mathbf{AB}^{-1}. \tag{15}$$

Again, the Legendre polynomials, $\mathcal{L}_{\alpha_i}(x_i) \in \mathcal{P}_{\alpha_i}$, are used with $\rho(x_i) = 1$ for all input dimensions $i = 1, ..., n$. Therefore, a vector of basis functions in one input dimension is

$$\boldsymbol{\phi}_i(x_i) = \begin{bmatrix} \mathcal{L}_{0_i}(x_i) \\ \mathcal{L}_{1_i}(x_i) \\ \vdots \\ \mathcal{L}_{\alpha_i}(x_i) \end{bmatrix}. \tag{16}$$

The complete basis function library, $\boldsymbol{\phi}(\mathbf{x}) : \mathcal{R}^n \to \mathcal{R}^{\alpha_1 \cdots \alpha_n}$ for the input $\mathbf{x} \in \mathcal{R}^n$ is the tensor product of each $\boldsymbol{\phi}_i(x_i)$ such that

$$\boldsymbol{\phi}(\mathbf{x}) = \boldsymbol{\phi}_1(x_1) \otimes \boldsymbol{\phi}_2(x_2) \otimes ... \otimes \boldsymbol{\phi}_n(x_n). \tag{17}$$

APPENDIX B

The stabilized continuation method shown here follows the works [29, 30]. In this formulation, the shooting method requires finding the solution to

$$\frac{\mathrm{d}}{\mathrm{d}s}\mathbf{F}(\mathbf{z}, s) = \frac{\partial \mathbf{F}}{\partial \mathbf{z}}\frac{\mathrm{d}\mathbf{z}}{\mathrm{d}s} + \frac{\partial \mathbf{F}}{\partial s} = \mathbf{0}, \tag{18}$$

where s is the continuation parameter, $\mathbf{F}(\mathbf{z}, s)$ defines the boundary conditions and $\mathbf{z}$ are the free variables. Convergence problems emerge if a poor initial guess is given, therefore a stabilizing term may be given to ensure error does not accumulate:

$$\frac{\partial \mathbf{F}}{\partial \mathbf{z}}\frac{\mathrm{d}\mathbf{z}}{\mathrm{d}s} + \frac{\partial \mathbf{F}}{\partial s} = \mathbf{A}_m\mathbf{F}(\mathbf{z}, s) + \boldsymbol{\nu}_s. \tag{19}$$

This may be transformed into an ordinary differential equation with respect to $\mathbf{z}$ such that

$$\frac{\mathrm{d}\mathbf{z}}{\mathrm{d}s} = \frac{\partial \mathbf{F}}{\partial \mathbf{z}}^{-1}\left[\mathbf{A}_m\mathbf{F}(\mathbf{z}, s) + \boldsymbol{\nu}_s - \frac{\partial \mathbf{F}}{\partial s}\right]. \tag{20}$$

The matrix $\mathbf{A}_m$ must be a Hurwitz matrix and acts as a linear feedback for the boundary condition error. The stabilizing term, $\boldsymbol{\nu}_s$, may be selected via the controllability Grammian, $\mathbf{W}_c$, such that the system is driven to $\mathbf{0}$ at s_f

$$\boldsymbol{\nu}_s(s) = e^{\mathbf{A}^T(s_f - s)}\underbrace{\left(\int_{s_0}^{s_f} e^{\mathbf{A}(\tau - s_0)}e^{\mathbf{A}^T(\tau - s_0)}\right)^{-1}}_{\mathbf{W}_c^{-1}} e^{\mathbf{A}(s_f - s_0)}\mathbf{F}(\mathbf{z}_0). \tag{21}$$

This allows for the use variable-step numerical integrators, such as MATLAB's *ode45* to be used to solve the system.

For the TPBVP posed in Equation (9), this means

$$\mathbf{F}(\mathbf{z}) = \begin{bmatrix} \tilde{x}_{PSS}(\mathbf{z}) - x_{PSS} \\ \tilde{y}_{PSS}(\mathbf{z}) - y_{PSS} \\ \dot{\tilde{y}}_{PSS}(\mathbf{z}) - \dot{y}_{PSS} \end{bmatrix} \qquad \mathbf{z} = \begin{bmatrix} \Delta v_x \\ \Delta v_y \\ \sigma \end{bmatrix}, \tag{22}$$

where $\tilde{}_{PSS}(\mathbf{z})$ is a flow of the CR3BP with respect to the guess $\mathbf{z}$.

REFERENCES

[1] The Future of Space 2060 & Implications for U.S. Strategy: Report on the Space Futures Workshop. Technical report, Air Force Space Command, September 2019.

[2] NASA's lunar exploration program overview, September 2020.

[3] Zhaoyu Pei, Jizhong Liu, Qian Wang, Yan Kang, Yongliao Zou, He Zhang, Yuhua Zhang, Huaiyu He, Qiong Wang, Ruihong Yang, et al. Overview of lunar exploration and international lunar research station. *Chinese Science Bulletin*, 65(24):2577–2586, 2020.

[4] XU Lin1 PEI Zhaoyu, ZOU Yongliao, and WANG Chi. China's lunar and deep space exploration program for the next decade (2020–2030). *Chin. J. Space Sci*, 40(5):5, 2020.

[5] Igor Mitrofanov, Lev Zelenyi, and Vladislav Tretyakov. Luna-28 mission for polar samples return, as the key element of the initial stage of Russian Lunar Program. In *EGU General Assembly Conference Abstracts*, page 8739, 2020.

[6] Vladislav Tretyakov, Igor Mitrofanov, and Lev Zeleniy. Russian Lunar Landers Luna-25 and Lna-27: Goals of the missions and scientific investigations at Moon Polar Regions. In *EGU General Assembly Conference Abstracts*, page 6753, 2020.

[7] Venkatesan Sundararajan. Indian lunar space exploration program-chandrayaan I and II missions. In *AIAA SPACE 2012 Conference & Exposition*, page 5324, 2012.

[8] M Ohtake, Y Karouji, Y Ishihara, R Nomura, H Inoue, H Shiraishi, H Mizuno, T Hoshino, and D Aso. Current status of the planned lunar polar exploration mission jointly studied by india and japan. In *Lunar and Planetary Science Conference*, number 2548, page 1840, 2021.

[9] M J Holzinger, C C Chow, and P Garretson. A Primer on Cislunar Space. White Paper, Air Force Research Lab, 2021.

[10] AFRL's Cislunar Highway Patrol System seeks industry collaboration.

[11] Mark Bolden, Timothy Craychee, and Erin Griggs. An evaluation of observing constellation orbit stability, low signal-to-noise, and the too-short-arc challenges in the cislunar domain. 2020.

[12] Russell P Patera. Space event detection method. *Journal of Spacecraft and Rockets*, 45(3):554–559, 2008.

[13] Marcus J Holzinger, Daniel J Scheeres, and Kyle T Alfriend. Object correlation, maneuver detection, and characterization using control distance metrics. *Journal of Guidance, Control, and Dynamics*, 35(4):1312–1325, 2012.

[14] Daniel P Lubey and Daniel J Scheeres. Identifying and estimating mismodeled dynamics via optimal control policies and distance metrics. *Journal of Guidance, Control, and Dynamics*, 37(5):1512–1523, 2014.

[15] Navraj Singh, Joshua T Horwood, and Aubrey B Poore. Space object maneuver detection via a joint optimal control and multiple hypothesis tracking approach. In *Proceedings of the 22nd AAS/AIAA Space Flight Mechanics Meeting*, volume 143, pages 843–862. Univelt San Diego, CA, 2012.

[16] D Joseph Mook and John L Junkins. Minimum model error estimation for poorly modeled dynamic systems. *Journal of Guidance, Control, and Dynamics*, 11(3):256–261, 1988.

[17] Zach Hall, David Schwab, Roshan Eapen, and Puneet Singla. Reachability-Based Approach for Search and Detection of Maneuvering Cislunar Objects. In *AIAA SCITECH 2022 Forum*, AIAA SciTech Forum, San Diego, CA & Virtual, January 2022. American Institute of Aeronautics and Astronautics.

[18] G. Tommei, A. Milani, and A. Rossi. Orbit determination of space debris: Admissible regions. *Celestial Mechanics and Dynamical Astronomy*, 97(4):289–304, April 2007.

[19] Kohei Fujimoto and Daniel J. Scheeres. Applications of the admissible region to space-based observations. *Advances in Space Research*, 52(4):696–704, August 2013.

[20] Victory Szebehely. *Theory of Orbit: The Restricted Problem of Three Bodies*. Elsevier, 1967.

[21] Andrew D Cox, Kathleen C Howell, and David C Folta. Transit and capture in the planar three-body problem leveraging low-thrust invariant manifolds. *Celestial Mechanics and Dynamical Astronomy*, 133(5):1–21, 2021.

[22] Gerard Gómez and JOSEP M Mondelo. The dynamics around the collinear equilibrium points of the RTBP. *Physica D: Nonlinear Phenomena*, 157(4):283–321, 2001.

[23] Michel Hénon. Numerical exploration of the restricted problem, V. *Astronomy and Astrophysics*, 1:223–238, 1969.

[24] Daniel J Grebow. *Trajectory Design in the Earth-Moon System and Lunar South Pole Coverage*. PhD thesis, Purdue University, 2010.

[25] Gerard Gómez, Wang S Koon, MW Lo, Jerrold E Marsden, Josep Masdemont, and Shane D Ross. Connecting orbits and invariant manifolds in the spatial restricted three-body problem. *Nonlinearity*, 17(5):1571, 2004.

[26] Roshan T Eapen, Kathleen C Howell, and Kyle T Alfriend. On the use of zero-momentum surfaces to identify transport opportunities to planar Lyapunov orbits. In *AAS/AIAA Spaceflight Mechanics Conference*, 2020.

[27] Wang Sang Koon, Martin W. Lo, Jerrold E. Marsden, and Shane D. Ross. *Dynamical Systems, the Three-Body Problem and Space Mission Design*. Marsden Books, 2011.

[28] B. F. Villac and D. J. Scheeres. Escaping Trajectories in the Hill Three-Body Problem and Applications. *Journal of Guidance, Control, and Dynamics*, 26(2):224–232, March 2003.

[29] Toshiyuki Ohtsuka and Hironori Fujii. Stabilized continuation method for solving optimal control problems. *Journal of Guidance, Control, and Dynamics*, 17(5):950–957, September 1994.

[30] Mihir Vedantam, Maruthi R. Akella, and Michael J. Grant. Multi-Stage Stabilized Continuation for Indirect Optimal Control of Hypersonic Trajectories. In *AIAA Scitech 2020 Forum*, Orlando, FL, January 2020. American Institute of Aeronautics and Astronautics.